Journal of the European Ceramic Society 42 (2022) 965–972

Contents lists available at ScienceDirect

Journal of the European Ceramic Society

journal homepage: www.elsevier.com/locate/jeurceramsoc

New model to tune the dielectric properties of dense and half-dense sintered polycrystalline cu-doped Ni–Zn ferrite

Nuria Vicente [a,b], Andres Mormeneo-Segarra [a], Carolina Clausell-Terol [a,b,*], Antonio Barba-Juan [a,b]

[a] Departamento de Ingeniería Química, Universitat Jaume I, 12071, Castellón, Spain
[b] Instituto Universitario de Tecnología Cerámica, Universitat Jaume I, 12071, Castellón, Spain

ARTICLE INFO

Keywords:
Complex electrical permittivity
Ni-Zn ferrites
High frequencymicrostructure
Magneto-dielectric

ABSTRACT

Sintered polycrystalline Cu-doped Ni–Zn ferrite specimens have been successfully prepared by a conventional ceramic method using different pressure-temperature-time cycles. The studied samples, with an average grain size of 5–25 μm and a porosity less than 0.20, exhibited a high effective complex permittivity-real part (ε'_{eff}) and a minimum dielectric loss above 1 GHz.

ε'_{eff} was successfully calculated using the Bruggeman-Landauer equation for the lowest angular frequencies and the Jayasundere-Smith equation for the highest one. To accurately predict the values of ε'_{eff}, both equations must be improved considering the Zheng approach. The need to change the model highlights the change in the polarization mechanism that occurs at high angular frequencies.

The two proposed modified equations allow predicting the ε'_{eff} for a dense and half-dense ferrite from its microstructure (porosity) and its constituent permittivities (grain and air).

1. Introduction

Nickel-zinc ferrites are magnetic materials of technological importance. Due to its high chemical stability, high resistivity, and excellent electromagnetic properties, they have a wide variety of electronic and magnetic applications, such as high-frequency communication components [1], microwave devices [2], multilayer chip inductors [3], electromagnetic shielding [4], energy storage, photocatalysis and sensors [5]. Furthermore, they are cost effective [6].

The fast progress of new electronic and mobile technologies requires increasingly smaller and lighter high-performance electronic devices, as well as inexpensive. In recent years, the ability of these materials to retain both permeability and permittivity simultaneously over a wide range of angular frequencies, has drawn the attention of the scientific community [7–9]. Effective multifunctional electronic materials can provide both capacitive and inductive performances, which are the key features in electrical circuits.

Optimal devices require ferrites with high initial permeability, low electrical conductivity and negligible eddy current losses [10]. Polycrystalline Cu-doped Ni–Zn ferrites are high-performance soft magnetic materials, exhibiting, as required, high complex initial permeability, low AC electric conductivity and appropriate permittivity over a wide range of angular frequencies [11,12].

Both magnetic and electrical properties of polycrystalline Ni-Zn ferrites are extremely depend to a great extent on the chemical composition and microstructure of the sintered bodies (grain size, bulk density, porosity, etc.), which in turn are determined by the preparation process (particle size of the starting powder, shaping conditions, and particularly sintering temperature, time and atmosphere) [5,10,19, 11–18].

Literature reports that the electrical properties of polycrystalline solids depend on the microstructure of the bodies, especially their porosity. However, very few studies can be found in the literature establishing a mathematical relationship between microstructure and electrical permittivity that is capable of accurately predicting the effective dielectric constant. Furthermore, none of these models has been tested over a wide range of porosities and angular frequencies.

The first studies were developed by Maxwell Garnett [20] and Bruggeman [21] in the first third of the 20th century, and by Landauer [22] in the early last quarter of the 20th century. These were focused on

* Corresponding author at: Departamento de Ingeniería Química, Universitat Jaume I, 12071, Castellón, Spain.
E-mail address: cclausel@uji.es (C. Clausell-Terol).

https://doi.org/10.1016/j.jeurceramsoc.2021.11.026
Received 24 September 2021; Received in revised form 6 November 2021; Accepted 10 November 2021
Available online 11 November 2021

low porosity two-phase composites and proposed several mathematical equations that relate dielectric properties to the volume fraction of the pores and the matrix. In 2020 Zheng [23] modified these equations, considering the Effective Medium Theory (EMT) and including an additional empirical parameter.

Other authors have taken different approaches. Liu [24] in 2016 proposed a general model that relates the dielectric constant with the porosity for any kind of porous material, but independent on the shape of the pores when the size of the pore is much smaller than the electromagnetic wavelength. A structural factor, β, is included to consider the through-hole and close-pore structure of the materials. This model has only been validated at low angular frequencies ranging from 10^3 Hz to 10^7 Hz. Jayasundere [25] in 1993 modified the Kerner equation [26] to adapt it to high porosity ceramics taking into account the effect of the applied field on the spheres and the surrounding.

In previous investigations, authors have stablished some mathematical correlations between the magnetic behaviour of a CuNiZn ferrite and its microstructure [27–30]. The aim of this paper is to establish a quantitative relationship between the real part of the effective complex electrical permittivity (ε'_{eff}) and the microstructure of this sintered polycrystalline ferrite to obtain bulk solids with a targeted permittivity, according with the well-known materials science triangle. A deeper study of the microstructure-permittivity relationship in Ni-Zn ferrites is shown, applying different theoretical models, comparing and improving them to incorporate the effect of the relative density (ϕ) in a single equation that could predict ε'_{eff}. The robustness of the mathematical model is the most remarkable characteristic given the wide range of porosity (between 0 and 0.5) and angular frequency at room temperature (from 10^6 to $2.5{\cdot}10^9$ Hz) in which it has been tested.

2. Experimental procedure

An homogeneous polycrystalline ferrite of chemical composition $(Cu_{0.12}Ni_{0.23}Zn_{0.65})Fe_2O_4$ (Fair-Rite Products Corp.; purity, 99.7 %) was used as starting powder. Fig. 1 shows its X-ray diffraction diagram which corresponds to the spinel crystalline structure according to the sets of ICDD (International Centre for Diffraction Data) powder diffraction files (PDF-4$^+$). In all the sintered samples, a single phase corresponding to the same spinel crystal structure was identified, showing an XRD diffractogram similar to that shown in Fig. 1.

Commercial powder consists of spray-dried granules, with an average size of 175 μm, made up of particles with an average size of 1–2 μm and a narrow particle-size distribution. Real density value of 5380 kg/m^3 was determined by helium pycnometer.

Cylindrical and toroidal test specimens (3 mm thick and 19 mm external diameter; 6 mm internal diameter for the toroidal test specimens) were shaped by uniaxial dry pressing and sintered by the conventional air solid-state method in an electric laboratory furnace.

Six compaction pressures, (50, 75, 200, 150, 200 and 300 MPa), ten sintering temperatures (900, 950, 975, 1000, 1025, 1050, 1075, 1100, 1150 and 1200 °C) and eleven sintering times (0, 5, 10, 20, 30, 45, 60, 120, 300, 900 and 1800 min) were used to obtain 594 samples (see Supplementary Tables 1–6) covering a wide range of relative densities and average grain sizes. This high number of samples was used in previous studies to determine the sintering kinetics of the ferrite and the mass transfer mechanisms that govern densification and grain growth [31]. These data have allowed to design an optimal thermal cycle (enhancing densification and controlling grain growth) to obtain the targeted sintered polycrystalline microstructure [32–34]. The authors have also developed a general procedure for determining the optimal thermal cycles of any ceramic based on the fundamentals of solid-state sintering [35].

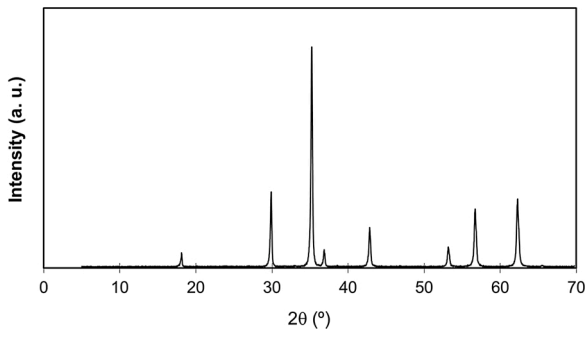

Fig. 1. X-ray diffraction pattern of the studied ferrite, corresponding to the Cu-Ni-Zn spinel crystalline structure.

Bulk densities of samples were measured according to Archimedes principle. Relative density (ϕ) of each sample was calculated as the ratio between bulk density and real density of the starting powder (5380 kg m^{-3}), from which porosity can be calculated as $P = 1 - \phi$. A scanning electron microscope (FEG-ESEM Quanta 200 F) was used to observe the microstructure of the ferrite specimens. Average grain size (G) was measured from the grain size distribution, determined by image analysis of the cross-sectional area of the rectangular thermal etched surface of each cylindrical sintered specimen, observed by scanning electron microscopy (SEM). The complex permittivity (real ε' and imaginary ε'' parts) was obtained in an Agilent E4991A RF impedance/material analyser in a frequency range between 10^6 Hz and $2.5{\cdot}10^9$ Hz, using an Agilent 16453A dielectric material test fixture.

A more detailed experimental procedure can be found in the authors' articles mentioned above.

3. Results and discussions

3.1. Microstructural considerations about ferrite bodies

Properties of Ni-Zn ferrites are determined not only by their chemical composition [16] but also by their microstructure, i.e. grain- and pore-size distribution, total porosity (or relative density) and grain-boundary characteristics. Final microstructure of specimens is given by the green body forming (conditioned by the particle size distribution of the starting powder [15]) and the sintering conditions (atmosphere, peak temperature and dwell time). The wide range of sintering conditions previously studied has yielded a large number of specimens with very different microstructures. By way of example, Fig. 2a and b show the various microstructures obtained using different pressing pressures, peak sintering temperatures and dwell sintering times. Fig. 2a shows the microstructure development for 30 min sintering time at two sintering temperatures (1000 and 1150°C) and six pressing pressures, while Fig. 2b shows the microstructure development for 60 min sintering time and 50 MPa pressing pressure at eight sintering temperatures. As noted above, sintering involves two simultaneous competitive processes: densification and grain growth. The higher the pressure, the temperature and/or the dwell time the higher the densification and grain growth. The kinetic equations of densification and grain growth were obtained from the experimental data of relative density and average grain size of each specimen. Furthermore, it was established that the boundary diffusion mass transfer mechanism controls the densification process and that grain growth is governed by surface diffusion pore drag control [31–34]. The established mathematical relationships allow the design of a suitable thermal cycle for the manufacture of ferrite pieces with maximum relative density (around 0.95) and limited grain growth (average grain size less than 25 μm) and, therefore, good electromagnetic properties [34,35].

The occurrence of crystalline precipitates was found when high peak sintering temperatures and/or dwell sintering times were used due to oxygen deficiency. This oxygen deficiency in turn depends on the microstructure of the sample. Thus, when the pore size distribution is finer and narrower, and the network formed between the particles is more tortuous, oxygen access becomes more difficult, reducing the

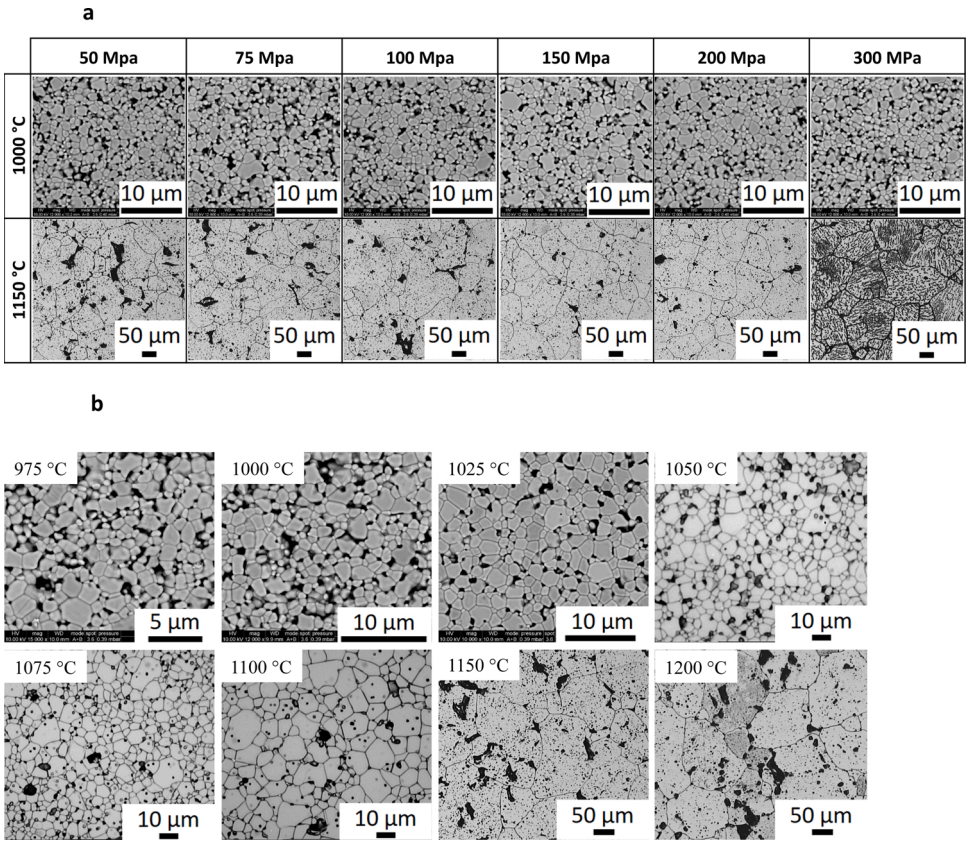

Fig. 2. a SEM images of the polished and etched cross-section areas of the sintered specimens uniaxial pressed at 50, 75, 100, 150, 200 and 300 MPa and two temperatures (1100 and 1150 °C) for 30 min. b SEM images of the polished and etched cross-section areas of the sintered specimens uniaxial pressed at 50 MPa and different temperatures (975, 1000, 1025, 1050, 1075, 1100, 1125 and 1150 °C) for 60 min.

oxygen concentration within the sample. Fig. 3 correspond to a cross-sectional SEM micrograph showing the sintered microstructure, with well-drawn grain boundaries, of a sample with crystalline precipitates. As concluded, initially rounded crystals are precipitated at the triple points, then at the grain boundaries and, finally, when the grain boundaries are saturated, within the grains. Smaller elongated crystals then precipitate around the previously formed ones. The former were identified as zinc oxide (ZnO) and the latter as copper oxide (CuO and Cu_2O) [36,37]. In all cases, crystal precipitation occurs when the average grain size is greater than 25 µm, worsening the electromagnetic performance of these ferrites.

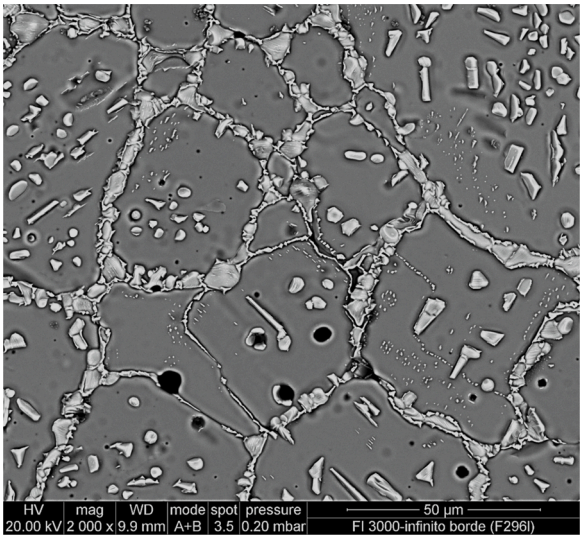

Fig. 3. Cross-sectional SEM micrograph showing the microstructure and grain boundaries of a $Cu_{0.12}Ni_{0.23}Zn_{0.65}Fe_2O_4$ sintered specimen with zinc oxide and copper oxide(s) crystal precipitates.

The microstructural properties and complex electrical permittivity (real part ε'_{eff}) at the four angular frequencies tested (10^6, 10^7, 10^8 and 10^9 Hz) of the 594 tested specimens of the sintered polycrystalline Cu-doped Ni-Zn ferrite are displayed in the Supplementary Tables 1–6. Only the 464 pieces that have an average grain size of less than 25 microns (and in which the devitrification mentioned in the previous paragraph has not occurred) have been used for the study presented in the following sections.

3.2. Qualitative analysis of electrical permittivity

Fig. 4a plots the experimental values of the electrical permittivity (real ε'_{eff} and imaginary parts, ε''_{eff}) of the $Cu_{0.12}Ni_{0.23}Zn_{0.65}Fe_2O_4$ ferrite versus the angular frequency (from 10^6 to $2.5{\cdot}10^9$ Hz). Only three curves are plotted, by way of example, corresponding to specimens with three different porosity ranges (0−0.1, 0.1−0.2 and 0.2−0.45 of porosity). Fig. 4b plots the experimental values of the dielectric loss tangent or dissipation factor (calculated as the ratio $\tan\delta_\varepsilon = \varepsilon''_{eff}/\varepsilon'_{eff}$) versus the angular frequency. It should be noted that the 464 specimens tested show a similar behaviour to the three specimens depicted in Fig. 4a and b, highlighting the dependence of electrical permittivity and dielectric loss tangent with porosity.

Fig. 4a shows that:

- ε'_{eff} decreases with porosity

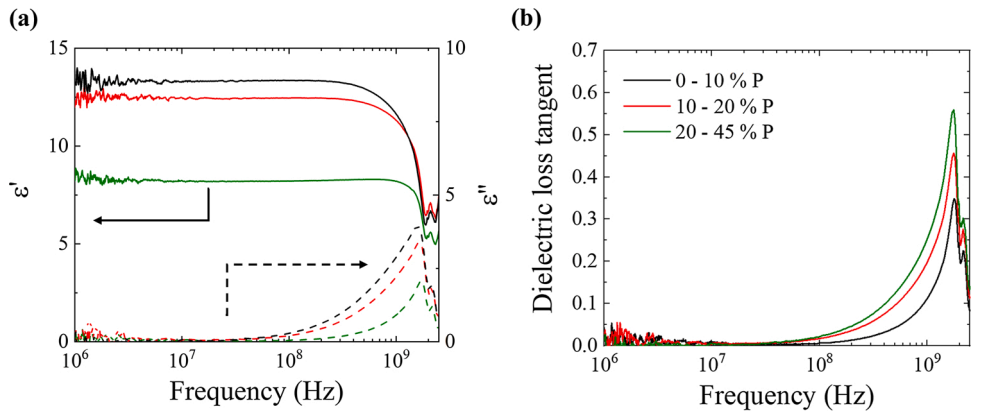

Fig. 4. Electric permittivity (real ε'_{eff} and imaginary ε''_{eff} parts) of $Cu_{0.12}Ni_{0.23}Zn_{0.65}Fe_2O_4$ ferrite versus the angular frequency (a) and the dielectric loss tangent or dissipation factor (calculated as the ratio $\tan[f_0]\delta_\varepsilon = \varepsilon''_{eff}/\varepsilon'_{eff}$) versus the angular frequency (b).

- ε'_{eff} is nearly constant at angular frequencies lower than 1 GHz, for all ranges of porosity, and it decreases sharply at higher frequencies (around 1.5 GHz), although the drop is less marked for the samples with high intragranular porosity (porosity in the range 0.2 – 0.45)
- ε'_{eff} is always higher than 5 in the range of angular frequencies of 10^6– 10^8 Hz
- ε'_{eff} shows successive peaks at angular frequencies above 1.5 GHz, caused by the change of polarization mechanism

This electrical property of the studied polycrystalline ferrite is a macroscopic reflection of the electronic polarization under the effect of the applied electric field. Typically, in polycrystalline ferrites, the electronic mechanism of polarization occurs due to electron jumps between Fe^{2+} and Fe^{3+} cations located at B-sites of the spinel crystalline lattice [38,39]. As a result, rotational displacements of Fe^{2+}/Fe^{3+} dipoles can align themselves with the direction of the alternating field, explaining the constant value of ε'_{eff} up to almost 1 GHz in Fig. 4a. However, at angular frequencies above 1 GHz, the exchange of electrons cannot follow the applied alternating field, so the polarization becomes determined mainly by the concentration of Fe^{2+}/Fe^{3+} ions in the B-sites [12,18,23].

As shown in Fig. 4a, ε''_{eff} exhibits relatively steady curves in the angular frequency range of 10^6 to 10^8 Hz, while it increases at higher angular frequencies showing a sharp peak above 10^9 Hz, usually attributed to the relaxation phenomenon [19]. Mathematically, the maxim value of ε''_{eff} is observed when the condition $\omega \bullet \tau = 1$ is fulfilled, where τ is the relaxation time and ω is the angular frequency calculated as $\omega = 2 \bullet \pi \bullet f$. This relaxation peak shifts towards lower frequencies when the average grain size (G) and / or the relative density (ϕ) increases.

Fig. 4b shows that the dielectric loss tangent increases with porosity (although it has also been found to increase with decreasing grain size [40]) and with angular frequency, up to a maximum, beyond which polarization falls off. This illustrates that the relaxation phenomenon is observed again around 1 GHz. The relaxation phenomenon or Debye relaxation is explained by the fact that the frequency of the applied electric field becomes approximately equal to the hopping frequency of the charge carriers, which means that a maximum transmission of the electrical energy to the electrons is taking place, appearing the loss peaks at resonance [18,41].

Hereinafter reference will only be made to the complex permittivity – real part values, since, as mentioned above, the curve remains virtually constant between 10^6 and 10^8 Hz. Additional information can be found in Supplementary Tables 1–6.

3.3. Quantitative analysis of electrical permittivity

Fig. 4a and b also reveal that electrical properties of the studied ferrite strongly depend on its heterogeneous microstructure and subsequently on the processing steps: synthesis of the powder, shaping technique, thermal sintering cycle, etc. There are several mathematical models in literature relating permittivity to porosity in polycrystalline materials [10]. Considering the CuNiZn ferrite studied as a two-phase composite (grains plus pores containing air) and the relatively high angular frequency tested in this work, only three models (previously mentioned in the introduction of this paper) can be remarked: Maxwell Garnett, Bruggeman-Landauer and Jasandure-Smith models, or MG, B–L and J–S models, respectively. All of them are based on the following assumptions:

a) specimen is composed of quasi-spherical crystalline particles and a gas phase (ferrite and air in our case), so it can be considered a dual-phase composite;
b) particle phase (ferrite particles) has a complex permittivity-real part of ε'_1;
c) gas phase has a complex permittivity-real part of ε'_2 ($\varepsilon'_2 = 1$ for air);
d) the volume fractions of the particles and the porous are $(1 - P)$ and P, respectively, fulfilling $(1 - P) + P = 1$;
e) when an electric field is applied to a polycrystalline material, the dielectric spheres are polarized and each one can be represented by a dipole moment which locally modifies the applied field in the surrounding medium according to the effective medium theory (EMT).

The Maxwell Garnett model [20] has been satisfactorily used to predict the electrical permittivity-real part in composites in which the volume fractions of the two phases differ greatly and one of the phases is uniformly and randomly dispersed in the other according to the following equation:

$$\varepsilon'_{calc} = \varepsilon'_1 \bullet \frac{2 \bullet \varepsilon'_1 + \varepsilon'_2 + 2 \bullet P \bullet (\varepsilon'_2 - \varepsilon'_1)}{2 \bullet \varepsilon'_1 + \varepsilon'_2 - P \bullet (\varepsilon'_2 - \varepsilon'_1)} \quad (1)$$

The Bruggeman-Landauer [21] model assumes that the typical non-uniform length scale in the microstructure is much smaller than the electromagnetic wavelength. Only the dipole interaction contributes to the polarization and all the details of the microstructure are included in the volume fraction parameter. According to this model, the calculation of the complex permittivity-real part of a biphasic-composite is done by the following equation:

$$(1 - P) \bullet \frac{\varepsilon'_1 - \varepsilon'_{calc}}{3 \bullet \varepsilon'_1 + 2 \bullet \varepsilon'_{calc}} + P \bullet \frac{\varepsilon'_2 - \varepsilon'_{calc}}{3 \bullet \varepsilon'_2 + 2 \bullet \varepsilon'_{calc}} = 0 \quad (2)$$

The Jasandure-Smith model [25] is an improvement of the

well-known Kerner [26] equation to estimate the dielectric constant including the interactions between neighbouring spheres (which are negligible only when porosity is very low), according to the equation:

$$\varepsilon'_{calc} = \frac{(1-P)\bullet\varepsilon'_1 + \frac{3\bullet\varepsilon'_1\bullet\varepsilon'_2\bullet P}{2\bullet\varepsilon'_1+\varepsilon'_2}\bullet\left[1+3\bullet P\bullet\frac{\varepsilon'_2-\varepsilon'_1}{\varepsilon'_2+2\bullet\varepsilon'_1}\right]}{(1-P)+\frac{3\bullet\varepsilon'_1\bullet P}{2\bullet\varepsilon'_1+\varepsilon'_2}\left[1+3\bullet P\bullet\frac{\varepsilon'_2-\varepsilon'_1}{\varepsilon'_2+2\bullet\varepsilon'_1}\right]} \quad (3)$$

In equations (1), (2) and (3):

ε'_{calc}: calculated effective complex permittivity-real part of the ferrite specimen

ε'_1: complex permittivity-real part of the pure ferrite

ε'_2: complex permittivity-real part of air

In this case, ε'_2 corresponds to the air trapped inside the pores ($\varepsilon'_2 = 1$), and ε'_1 has been calculated using Shannon's equation for simple oxides [42]:

$$\varepsilon'_1 = \frac{3\bullet V_m + 8\bullet\pi\bullet\alpha}{3\bullet V_m - 4\bullet\pi\bullet\alpha} \quad (4)$$

Were α is the total dielectric ionic polarizability and V_m is the molar volume in Å^3. For the $Cu_{0.12}Ni_{0.23}Zn_{0.65}Fe_2O_4$ ferrite $\alpha = 14.47$ (as the average of polarizabilities of the components) and $V_m = 73.07$ Å^3. Applying equation (4) a value of $\varepsilon'_1 = 15.62$ is obtained, which is in agreement with the value of the sintered bulk spinel ferrites ($\varepsilon'_1 = 15.80$) [42].

a) Testing equations (1), (2) and (3)

Fig. 5a depicts the experimental values of ε'_{eff} (black dots) versus porosity for all the 464 studied specimens at the angular frequency of 10^8 Hz, which is virtually the same for the angular frequencies of 10^6 and 10^7 Hz because ε'_{eff} remains practically constant in the frequency range of 10^6–$2{\cdot}10^8$ Hz. Fig. 5b shows the same representation at 10^9 Hz. The corresponding experimental data can be found in the Supplementary Tables 1–6. Solid lines in Fig. 5a and b depict the calculated values of ε'_{calc} by equations (1), (2) and (3), taking $\varepsilon'_1 = 15.62$ (obtained by Shannon's equation).

Calculated values are close to experimental ones for the densest specimens and, mainly, for the angular frequencies of 10^6, 10^7 and 10^8 Hz. Equations (1), (2) and (3) start to fail fitting experimental data when porosity is higher than 0.1 (Fig. 5a). At the angular frequency of 10^9 Hz, equations (1), (2) and (3) do not fit experimental values (Fig. 5b). The correlation coefficient, residue standard deviation and mean square error, shown in Supplementary Tables 7–10, were employed to quantify the differences between the measured and calculated complex permittivity-real part. The observed deviations between the calculated and experimental values could be explained by different reasons [43]. Higher total porosity result in a) higher trapped air, which has a low dielectric constant ($\varepsilon'_2 = 1$); b) lower number of grain-grain interfaces, decreasing the accumulation of charges at the interfaces; and c) smaller grain size. Consequently, the constant permittivity ε'_1 used in the EMT models does not reflect the contribution of small grains to the effective permittivity and a proper correction of ε'_1 is required.

b) Testing equations (1), (2) and (3) following Zheng proposal

Zheng [23] modified equations (1) and (2) introducing a dynamic modifying factor to correct the permittivity of the solid phase taking into account the grain size. Due to the close relationship between grain size and porosity, Zheng supposed a variation of ε'_1 with porosity according with the following equation:

$$\varepsilon'_1 = \varepsilon'_m \bullet \phi^{\beta} = \varepsilon'_m \bullet (1-P)^{\beta} \quad (5)$$

where:

ε'_m: complex permittivity-real part of a single crystal of solid phase

ϕ: relative density of the body

P: porosity

β: empirical correlation constant

Fig. 6a and c show again the experimental values of ε'_{eff} (black dots) versus porosity for all the 464 studied specimens, at the angular frequency of 10^8 Hz (which is virtually the same for the angular frequencies of 10^6 and 10^7 Hz because ε'_{eff} remains constant in the frequency range of 10^6–$2{\cdot}10^8$ Hz). Fig. 6b and d show the same representation at 10^9 Hz. The plotted experimental data can be found in the Supplementary Tables 1–6.

Solid lines in Fig. 6a–d depict the calculated values of ε'_{calc} by equations (1), (2) and (3) using equation (5) to calculate ε'_1. In equation (5) ε'_m can take the value of 15.62 (Fig. 6a and b) or be treated as an adjusting parameter (Fig. 6c and d). A nonlinear least-squares method has been used to fit data to equations (1), (2), (3) and (5), allowing the estimation of constants β and ε'_m (if applicable), by minimizing the sum of squared residuals. The calculated effective complex electrical permittivity-real part can be estimated by substituting the previously obtained β and ε'_m (if applicable) constants in the corresponding equations. As can be observed, the calculated values of the complex permittivity-real part using equation (2) proposed by Burggeman-Landauer, or equation (3) proposed by Jayasundere-Smith, and both modified by Zheng, are in good agreement with the experimental results in the wide range of porosities tested. Less satisfactory agreement was found in the results obtained with equation (1) proposed by Maxwell Garnett and modified by Zheng.

Table 1 shows the calculated values of ε'_m and β to fit the experimental data in the four tested angular frequencies. The value of β changes in every model, remaining constant for the angular frequencies of 10^6, 10^7 and 10^8 Hz and increasing at the angular frequency of 10^9, due to the change in the polarization mechanism. Additional

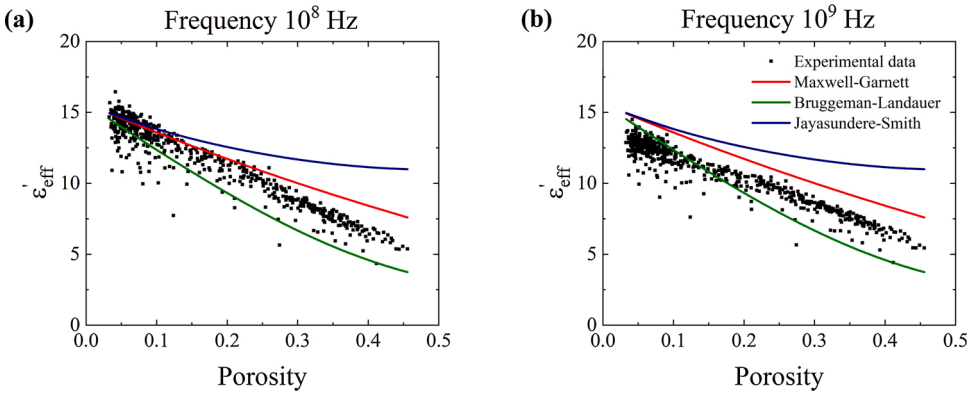

Fig. 5. ε'_{eff} (black dots) versus porosity for all the 464 studied specimens, at the angular frequency of 10^8 Hz (a) and 10^9 Hz (b). Solid lines correspond to the calculated values of ε'_{calc} by equations (1), (2) and (3), taking $\varepsilon'_1 = 15.62$.

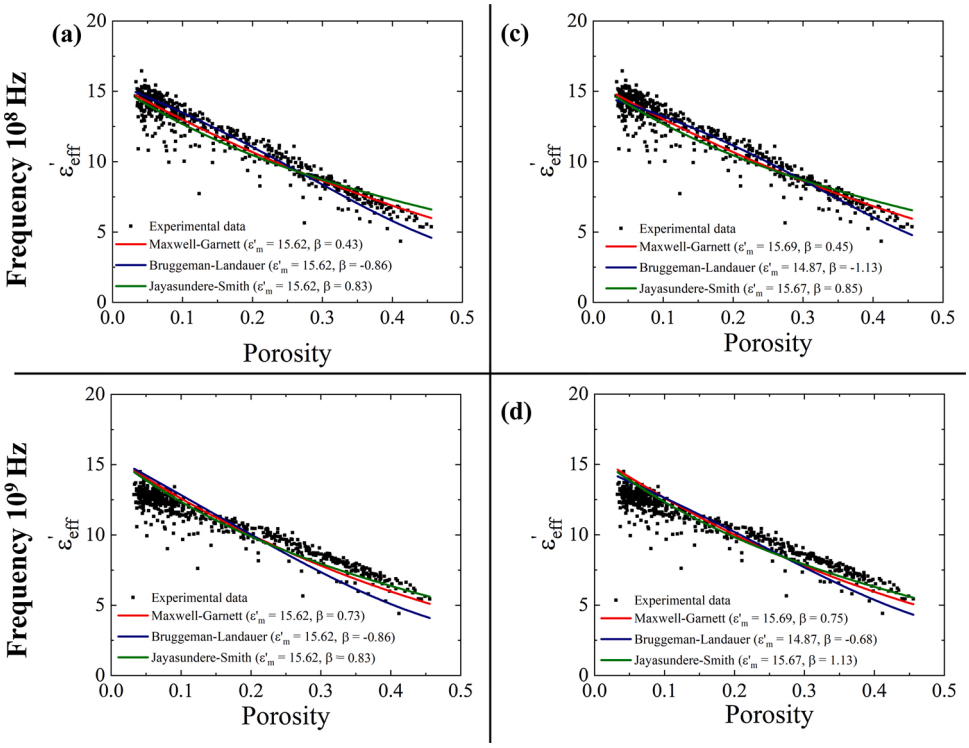

Fig. 6. ε'_{eff} (black dots) versus porosity for all the 464 studied specimens, at the angular frequency of 10^8 Hz (a and c) and 10^9 Hz (b and d). Solid lines correspond to the calculated values of ε'_{calc} by equations (1), (2) and (3) considering equation (5) to calculate ε'_1 ; in equation (5) ε'_1 can take the value of 15.62 (a and b) or be treated as an adjusting parameter (c and d).

information is found in Supplementary Tables 7–10.

Fig. 6 shows that the three models satisfactorily reproduce the experimental data trend in almost the entire range of porosities and grain sizes, and for the four angular frequencies tested, although a better linear fit was obtained at low angular frequencies (10^6, 10^7 and 10^8 Hz). Results improve when ε'_m is estimated instead of taking the value of 15.62, (Fig. 6a and c), yielding a very good agreement between the calculated and experimental values. The best agreement is achieved using the Burggeman-Landauer model modified by Zheng, equations (2) and (5), with $\varepsilon'_m = 14.87$. This ε'_m value corresponds to the largest deviation (Table 1) of the value calculated using the Shannon equation but, even in this case, it is considered acceptable. In the angular frequency of 10^9 Hz, the Jayasundere-Smith model modified by Zheng (equations (3) and (5)) provides the best agreement between the experimental and calculated values, probably because it considers the interaction of neighboring spheres.

Fig. 7a shows the values of the calculated complex electrical permittivity-real part (using equations (2) and (5) and the corresponding ε'_m and β values from Table 1) versus the experimental ones for the angular frequency of 10^8 Hz (this plot is virtually the same for the angular frequencies of 10^6 and 10^7 Hz because ε'_{eff} remains constant in the frequency range of 10^6–$2{\cdot}10^8$ Hz). Fig. 7a also shows the goodness of the linear fit between ε'_{eff} and ε'_{calc}, with a slope-1 line passing through the coordinate origin and a high correlation coefficient (see Supplementary Table 9). As can be observed, the modified Burggeman-Landauer model allows to reproduce the experimental data accurately, giving a good random localization of the experimental data around the slope-1 line.

Fig. 7b shows the calculated complex electrical permittivity-real part values (using equations (3) and (5) and the corresponding ε'_m and β values from Table 1) versus the experimental ones, for the angular frequency of 10^9 Hz. Fig. 7b also shows the goodness of the linear fit between ε'_{eff} and ε'_{calc}, with a slope-1 line passing through the coordinate origin and a high correlation coefficient (see Supplementary Table 10). As can be observed, the modified Jayasundere-Smith model allows to reproduce the experimental data accurately, giving a good random localization of data points around the slope-1 line.

The simulated dielectric constant results obtained for the modified Burggeman-Landauer model at 10^9 Hz, for the modified Jayasundere-Smith model at 10^8 Hz and for the modified Maxwell Garnett model at 10^8 and 10^9 Hz are shown in Supplementary Fig. 1. As can be seen in these figures, although the results obtained for these four cases are quite good, they are slightly worse than those obtained for the modified Burggeman-Landauer model at 10^8 Hz and for the modified Jayasundere-Smith model at 10^9Hz (Fig. 7a and b). Therefore, the model of Burggeman-Landauer, for low frequencies, and the model of Jayasundere-Smith, for high frequencies, both suitably modified by Zheng equation, have proven to be the best tool for predicting dielectric properties of dense and half-dense ferrites.

Table 1
Values of ε'_m and β used for fitting experimental data at different angular frequencies.

Equations	ε'_m	$\omega = 10^6, 10^7, 10^8$ Hz β	$\omega = 10^9$ Hz β
(1) and (5) (Maxwell Garnett modified by Zheng)	15.62	0.43	0.75
	15.69	0.45	0.75
(2) and (5) (Burggeman-Landauer modified by Zheng)	15.62	−0.86	−0.86
	14.87	−1.13	−0.68
(3) and (5) (Jayasundere-Smith modified by authors with Zheng equation)	15.62	0.83	0.83
	15.67	0.85	1.13

4. Conclusions

Sintered polycrystalline Cu-doped Ni–Zn ferrite specimens have been successfully prepared by conventional ceramic method using different

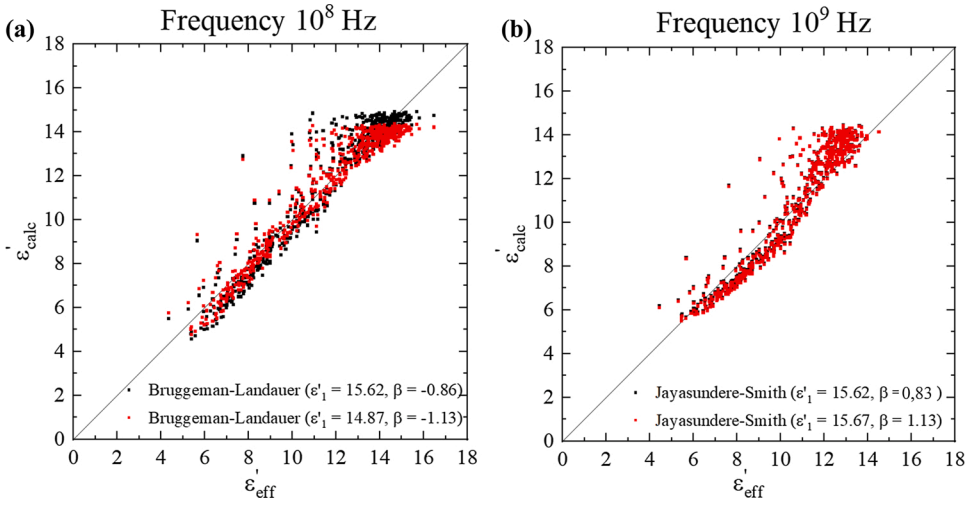

Fig. 7. Calculated complex electric permittivity-real part values (using equations (2) and (5) and the corresponding $\varepsilon_m^{'}$ and β values from Table 1) versus the experimental ones for the angular frequency of 10^8 Hz (a) and (using equations (3) and (5) and the corresponding $\varepsilon_m^{'}$ and β values from Table 1) for the angular frequency of 10^9 Hz (b).

pressure-temperature-time cycles, yielding 594 bodies with a wide range of porosities (from near-zero to 0.45) and average grain sizes (from 1 to 150 μm). Of these 594 specimens, 464 have an average grain size in the range of 5–25 μm, a porosity of less than 0.20, and a single crystalline phase, corresponding to the spinel ferrite. Likewise, they exhibit a high effective complex permittivity-real part, around 15 and virtually constant in the angular frequency range of 10^6 – 10^8 Hz, while the minimum dielectric loss is above 1 GHz.

The effective complex permittivity-real part of the studied ferrite has been accurately calculated using the model of Bruggeman-Landauer, suitably modified considering the Zheng approach, in the range of angular frequencies of 10^6-10^8 Hz. However, for the value of the angular frequency of 10^9 Hz, the Jayasundere-Smith model, also including the Zheng approach, allowed to reproduce more precisely the values of the effective complex permittivity-real part. The need to change the model beyond 10^9 Hz angular frequency highlights the change in the polarization mechanism that occurs at high angular frequency.

The good behavior of both models in a wide range of porosities leads to the conclusion that the effective complex permittivity-real part can be predicted for a dense and half-dense ferrite from its microstructure (porosity) and constituent permittivities (grain and gas phase, which are ferrite and air in our case) in a wide range of frequencies. But, depending on the polarization mechanism, the appropriate model must be used.

Declaration of Competing Interest

The authors reported no declarations of interest.

Acknowledgments

This study has been supported by Ministerio de Economía y Competitividad (Spain) through grant number (MAT2016–76320-R) and by Universitat Jaume I (Spain), grant numbers (UJIB2017-48, UJIB2020-13 and POSDOC/2020/04). Complex relative permittivity determination was carried out at the central facilities (Servei Central d'Instrumentació Científica) of the Universitat Jaume I (Spain).

Appendix A. Supplementary data

Supplementary material related to this article can be found, in the online version, at doi:https://doi.org/10.1016/j.jeurceramsoc.2021.11.026.

References

[1] N. Parsa, R.C. Toonen, Ferromagnetic nanowires for nonreciprocal millimeter-wave applications: Investigations of artificial ferrites for realizing high-frequency communication components, IEEE Nanotechnol. Mag. 12 (2018), https://doi.org/10.1109/MNANO.2018.2869234.
[2] C. Stergiou, Magnetic, dielectric and microwave absorption properties of rare earth doped Ni–Co and Ni–Co–Zn spinel ferrites, J. Magn. Magn. Mater. 426 (2017) 629–635, https://doi.org/10.1016/j.jmmm.2016.11.001.
[3] R. Jasrotia, P. Puri, A. Verma, V.P. Singh, Magnetic and electrical traits of sol-gel synthesized Ni-Cu-Zn nanosized spinel ferrites for multi-layer chip inductors application, J. Solid State Chem. 289 (2020) 121462, https://doi.org/10.1016/j.jssc.2020.121462.
[4] D. Venkatesh, K.V. Ramesh, Structural and electrical properties of Cu-doped Ni-Zn nanocrystalline ferrites for MLCI applications, Mod. Phys. Lett. B 31 (2017) 1750318, https://doi.org/10.1142/S0217984917503183.
[5] S. Sharifi, A. Yazdani, K. Rahimi, Incremental substitution of Ni with Mn in NiFe2O4 to largely enhance its supercapacitance properties, Sci. Rep. 10 (2020) 10916, https://doi.org/10.1038/s41598-020-67802-z.
[6] M. Sugimoto, The Past, Present, and future of ferrites, J. Am. Ceram. Soc. 82 (1999) 269–280, https://doi.org/10.1111/j.1551-2916.1999.tb20058.x.
[7] J.L. Mattei, E. Le Guen, A. Chevalier, Dense and half-dense NiZnCo ferrite ceramics: their respective relevance for antenna downsizing, according to their dielectric and magnetic properties at microwave frequencies, J. Appl. Phys. 117 (2015), https://doi.org/10.1063/1.4913700.
[8] X. Wu, Z. Zheng, Q. Feng, Investigations on the microwave-absorbing properties of NiZnCo magneto-dielectric ferrites, 2019 Int. Appl. Comput. Electromagn. Soc. Symp. ACES 2019 (2019), https://doi.org/10.23919/ACES48530.2019.9060605.
[9] Z. Zheng, Y. Li, T. Liu, Q. Feng, Novel high-frequency magneto-dielectric properties of CaO-SiO2 Co-doped NiZnCo spinel ferrites for RF and microwave device applications, IEEE Trans. Magn. 54 (2018) 2801404, https://doi.org/10.1109/TMAG.2018.2847563.
[10] M. Harun-Or-Rashid, M.N. Islam, M. Arifuzzaman, A.K.M.A. Hossain, Effect of sintering temperature on the structural, morphological, electrical, and magnetic properties of Ni–Cu–Zn and Ni–Cu–Zn–Sc ferrites, J. Mater. Sci. Mater. Electron. 32 (2021) 2505–2523, https://doi.org/10.1007/s10854-020-05018-7.
[11] A.V. Humbe, P.B. Kharat, A.C. Nawle, K.M. Jadhav, Nanocrystalline Ni0.70−xCuxZn0.30Fe2O4 with $0 \leq x \leq 0.25$ prepared by nitrate-citrate route: structure, morphology and electrical investigations, J. Mater. Sci. Mater. Electron. 29 (2018) 3467–3481, https://doi.org/10.1007/s10854-017-8281-8.
[12] A. Afzal, F.A. Abuilaiwi, R. Javaid, F. Ali, A. Habib, Solid-state synthesis of heterogeneous Ni0.5Cu0.5-xZnxFe2O4 spinel oxides with controlled morphology and tunable dielectric properties, J. Mater. Sci. Mater. Electron. 31 (2020) 14261–14270, https://doi.org/10.1007/s10854-020-03982-8.
[13] A. Verma, D.C. Dube, Processing of nickel-zinc ferrites via the citrate precursor route for high-frequency applications, J. Am. Ceram. Soc. 88 (2005) 519–523, https://doi.org/10.1111/j.1551-2916.2005.00098.x.
[14] T.T. Ahmed, I.Z. Rahman, M.A. Rahman, Study on the properties of the copper substituted NiZn ferrites, J. Mater. Process. Technol. 153–154 (2004) 797–803, https://doi.org/10.1016/j.jmatprotec.2004.04.188.
[15] A. Hajalilou, H.M. Kamari, K. Shameli, Dielectric and electrical characteristics of mechanically synthesized Ni-Zn ferrite nanoparticles, J. Alloys. Compd. 708 (2017) 813–826, https://doi.org/10.1016/j.jallcom.2017.03.030.
[16] A. Hajalilou, S.A. Mazlan, K. Shameli, A comparative study of different concentrations of pure Zn powder effects on synthesis, structure, magnetic and

microwave-absorbing properties in mechanically-alloyed Ni-Zn ferrite, J. Phys. Chem. Solids 96–97 (2016) 49–59, https://doi.org/10.1016/j.jpcs.2016.05.001.
[17] C.A. Stergiou, V. Zaspalis, Analysis of the complex permeability of NiCuZn ferrites up to 1 GHz with regard to Cu content and sintering temperature, Ceram. Int. 40 (2014) 357–366, https://doi.org/10.1016/j.ceramint.2013.06.010.
[18] K.M. Batoo, Structural and electrical properties of Cu doped NiFe2O 4 nanoparticles prepared through modified citrate gel method, J. Phys. Chem. Solids 72 (2011) 1400–1407, https://doi.org/10.1016/j.jpcs.2011.08.005.
[19] E. Rezlescu, L. Sachelarie, P.D. Popa, N. Rezlescu, Effect of substitution of divalent ions on the electrical and magnetic properties of Ni-Zn-Me ferrites, IEEE Trans. Magn. 36 (2000) 3962–3967, https://doi.org/10.1109/20.914348.
[20] J.C. Maxwell Garnett, J. Larmor, Colours in metal glasses and in metallic films, Proc. R. Soc. London. 73 (1904) 443–445, https://doi.org/10.1098/rspl.1904.0058.
[21] V.D.A.G. Bruggeman, Calculation of various physics constants in heterogenous substances I Dielectricity constants and conductivity of mixed bodies from isotropic substances, Ann. Phys. 24 (1935).
[22] R. Landauer, Electrical conductivity in inhomogeneous media, AIP Conf. Proc. 40 (1978) 2–45, https://doi.org/10.1063/1.31150.
[23] Z. Zheng, X. Wu, Q. Feng, V.G. Harris, Low loss and tailored high-frequency performances of BaO-doped NiZnCo magneto-dielectric ferrites, J. Am. Ceram. Soc. 103 (2020) 1248–1257, https://doi.org/10.1111/jace.16831.
[24] X. Da Liu, Z.L. Hou, B.X. Zhang, K.T. Zhan, P. He, K.L. Zhang, W.L. Song, A general model of dielectric constant for porous materials, Appl. Phys. Lett. 108 (2016) 102902, https://doi.org/10.1063/1.4943639.
[25] N. Jayasundere, B.V. Smith, Dielectric constant for binary piezoelectric 0-3 composites, J. Appl. Phys. 73 (1993) 2462–2466, https://doi.org/10.1063/1.354057.
[26] E.H. Kerner, The electrical conductivity of composite media, Proc. Phys. Soc. Sect. B. 69 (1956) 802–807, https://doi.org/10.1088/0370-1301/69/8/304.
[27] A. Barba-Juan, N. Vicente, A. Mormeneo-Segarra, C. Clausell-Terol, Influence of microstructure and magnetizing mechanisms on magnetic complex permeability (imaginary part) of a Cu-doped Ni–Zn polycrystalline ferrite, Ceram. Int. (2021), https://doi.org/10.1016/j.ceramint.2021.07.119.
[28] A. Barba, C. Clausell, J.C. Jarque, L. Nuño, Magnetic complex permeability (imaginary part) dependence on the microstructure of a Cu-doped Ni–Zn-polycrystalline sintered ferrite, Ceram. Int. 46 (2020) 14558–14566, https://doi.org/10.1016/j.ceramint.2020.02.255.
[29] C. Clausell, A. Barba, L. Nuño, J.C. Jarque, Effect of average grain size and sintered relative density on the imaginary part - μ″ of the complex magnetic permeability of (Cu0.12Ni0.23Zn0.65)Fe2O4 system, Ceram. Int. 42 (2016) 4256–4261, https://doi.org/10.1016/j.ceramint.2015.11.101.
[30] C. Clausell, A. Barba, L. Nuño, J.C. Jarque, Electromagnetic properties of ferrite tile absorber as a function of compaction pressure, Ceram. Int. 42 (2016) 17303–17309, https://doi.org/10.1016/j.ceramint.2016.08.026.
[31] A. Barba, C. Clausell, C. Felíu, M. Monzó, Sintering of (Cu0.25Ni0.25Zn0.50)Fe2O4 ferrite, J. Am. Ceram. Soc. 87 (2004) 571–577, https://doi.org/10.1111/j.1551-2916.2004.00571.x.
[32] A. Barba, C. Clausell, M. Monzó, J.C. Jarque, Thermal cycle for obtaining a Ni-Zn ferrite: (I) Design of the sintering stage, Bol. La Soc. Esp. Ceram. y Vidr. 47 (2008) 13–23.
[33] A. Barba, C. Clausell, M. Monzó, J.C. Jarque, Thermal cycle for obtaining a Ni-Zn ferrite: (II) Influence of the cooling stage, Bol. La Soc. Esp. Ceram. y Vidr. 47 (2008) 101–104.
[34] C. Clausell, A. Barba, Processing–microstructure–properties relationship in a CuNiZn ferrite, Bol. La Soc. Esp. Ceram. y Vidr. 57 (2018) 29–39, https://doi.org/10.1016/j.bsecv.2017.09.002.
[35] A. Barba-Juan, C. Clausell-Terol, A general method to determine optimal thermal cycles based on solid-state sintering fundamentals, Ceram. Int. 45 (2019) 5346–5354, https://doi.org/10.1016/j.ceramint.2018.11.233.
[36] A. Barba, C. Clausell, J.C.J.C. Jarque, M. Monzó, ZnO and CuO crystal precipitation in sintering Cu-doped Ni-Zn ferrites. I. Influence of dry relative density and cooling rate, J. Eur. Ceram. Soc. 31 (2011) 2119–2128, https://doi.org/10.1016/j.jeurceramsoc.2011.05.007.
[37] A. Barba, C. Clausell, L. Nuño, J.C.J.C. Jarque, ZnO and CuO crystal precipitation in sintering Cu-doped Ni-Zn ferrites. II. Influence of sintering temperature and sintering time, J. Eur. Ceram. Soc. 37 (2017) 169–177, https://doi.org/10.1016/j.jeurceramsoc.2016.07.033.
[38] L.L. Hench, J.K. West, Principles of Electronic Ceramics, Wiley, 1990. http://books.google.com.co/books?id=vQBTAAAAMAAJ.
[39] N. Rezlescu, E. Rezlescu, Dielectric properties of copper containing ferrites, Phys. Status Solidi 23 (1974) 575–582, https://doi.org/10.1002/pssa.2210230229.
[40] N. Sivakumar, A. Narayanasamy, N. Ponpandian, G. Govindaraj, Grain size effect on the dielectric behavior of nanostructured Ni 0.5Zn0.5Fe2O4, J. Appl. Phys. 101 (2007) 084116, https://doi.org/10.1063/1.2721379.
[41] N. Singh, A. Agarwal, S. Sanghi, Dielectric relaxation, conductivity behavior and magnetic properties of Mg substituted Zn-Li ferrites, Curr. Appl. Phys. 11 (2011) 783–789, https://doi.org/10.1016/j.cap.2010.11.073.
[42] R.D. Shannon, Dielectric polarizabilities of ions in oxides and fluorides, J. Appl. Phys. 73 (1993) 348–366, https://doi.org/10.1063/1.353856.
[43] B. Luo, X. Wang, Y. Wang, L. Li, Fabrication, characterization, properties and theoretical analysis of ceramic/PVDF composite flexible films with high dielectric constant and low dielectric loss, J. Mater. Chem. A. 2 (2014) 510–519, https://doi.org/10.1039/c3ta14107a.